


The EUMETSAT Satellite Application Facility on Land Surface Analysis (LSA SAF)

Algorithm Theoretical Basis Document (ATBD)

Land Surface Albedo

PRODUCTS: LSA-103 (ETAL)

DOCUMENT SIGNATURE TABLE

	Name		
Prepared by :	Météo-France / CNRM	25/11/2016	
Approved by :	Land SAF Project Manager	25/11/2016	

DOCUMENTATION CHANGE RECORD

Issue / Revision	Date	Description:
Version 1.0	09/11/2012	
Version 1.1	04/03/2014	
Version 1.2	10/06/2016	Version prepared for ORR of the LSA System I - EPS and EPS Products
Version 1.3	25/11/2016	Version updated from ORR of the LSA System I - EPS and EPS Products

DISTRIBUTION LIST

Internal Consortium Distribution		
Organisation	Name	No. Copies
IPMA	Isabel Trigo	
	Sandra Coelho	
	Carla Sofia Barroso	
	Isabel Monteiro	
	João Paulo Martins	
	Pedro Diegues	
	Pedro Ferreira	
	Ana Veloso	
IDL	Carlos da Camara	
	Teresa Calado	
MF	Jean-Louis Roujean	
	Dominique Carrer	
RMI	Françoise Meulenberghs	
	Arboleda Alirio	
	Nicolas Ghilain	
KIT	Folke Olesen	
	Frank. Goettsche	
UV	Joaquin Melia	
	Fernando Camacho	
	F. Javier García Haro	
	Aleixandre Verger	

External Distribution		
Organisation	Name	No. Copies
EUMETSAT	Frédéric Gasiglia	
	Cleber Gomes Balan	
	Lorenzo Sarlo	
	Lothar Schueller	
EDISOFT	Teresa Cardoso	
EDISOFT	Joana Rosa	
EDISOFT	Joaquim Araújo	
GMV	Mauro Lima	

Steering Group Distribution		
Nominated by:	Name	No. Copies
IPMA	Pedro Viterbo	
MF	Jean-François Mahfouf	
RMIB	Rafiq Hamdi	
KIT	Johannes Orphal	
VITO	Bart Deronde	
EUMETSAT	Lothar Schueller	
	Harald Rothfuss	
	Christopher Hanson	
STG/AFG	Francesco Zauli	

Table of Contents

1 The EUMETSAT SAF on Land Surface Analysis.....	8
2 Introduction.....	10
3 Theoretical framework.....	13
4 Algorithm description.....	15
4.1 Overview.....	15
4.2 Atmospheric correction.....	17
4.3 Albedo calculation.....	19
4.3.1 Inversion method.....	19
4.3.2 Surface BRDF model.....	22
4.3.3 Weighting of measurements.....	23
4.3.4 Illustration of the model inversion.....	24
4.3.5 Temporal composition.....	25
4.3.6 Angular integration.....	27
4.4 Narrow- to Broad-band Conversion.....	29
4.5 Signification of the Uncertainty Estimates.....	30
4.6 The CAMS climatology used for aerosols correction.....	31
4.7 Residual effects of cloud masking.....	32
4.8 Synthesizing MDAL/MTAL and ETAL differences.....	34
4.8.1 Spectral resolution.....	34
4.8.2 Spatial resolution and projection.....	34
4.8.3 Directional resolution.....	35
4.8.4 Temporal resolution.....	35
5 Known issues and limitations.....	36
6 References.....	38
Appendix A - Developers.....	41
Appendix B - Glossary.....	41

List of Figures

Figure 1: Flow chart of the algorithm for atmospheric correction, BRDF model inversion, and albedo determination.....	17
Figure 2: Illumination (left) and observation (right) geometries corresponding to a geographical location of [47° 47' N, 10° 37' E] and an observation period between the days of year 150 and 170. The relative azimuth angle is identical for the two graphs. The convention was chosen such that the top of the graphs (=0°) corresponds to the back scattering regime. The colors of the dots denote observations taken by different sensors as follows: Red: SEVIRI/MSG, Green: AVHRR/METOP, Blue: AVHRR/NOAA. 19	
Figure 3: Angular dependence of the geometric (left) and volumetric (right) scattering kernels of the reflectance model introduced by Roujean et al. (1992). Negative zenith angle values correspond to the back scattering direction (relative azimuth angle =0°) and positive zenith angle values to the forward scattering direction (=180°).....	22
Figure 4: Dependence of the 0.8 µm-channel reflectance factor on the direction of the outgoing light ray for different incidence directions according to the model uncertainty.....	25
Figure 5: Effective temporal weight function in the recursive composition scheme. The characteristic time scale is = 10 days for AVHRR.....	26
Figure 6: Illumination zenith angle dependence of the directional-hemispherical kernel integrals for the Roujean et al. (1992) model.....	27
Figure 7: Dependence of the directional-hemispherical albedo on the illumination zenith angle. The value at the reference angle and the bi-hemispherical estimate are indicated.....	28
Figure 8: The colour contour image of CAMS climatology of AOD for September 6 h. The image is on a projected grid 0° West to 360° East and -90° South to 90° South... 	32
Figure 9: Sketch of the technique applied for the removal of cloud-contaminated pixels as a function of the solar geometry. Three examples are given here to discard nearest neighbour pixels (blue squares) relative to a cloudy pixel, according to the solar azimuthal position.....	33
Figure 10: Comparison of the spectral albedo for SEVIRI and AVHRR from simulations using the SAIL code (<i>van Leeuwen and Roujean, 2002</i>).....	34
Figure 11: Directional sampling from GEO (MSG/SEVIRI) and LEO (Metop/AVHRR) satellites for the city of Toulouse (France) on July 14, 2010, with plus/less 5 days for LEO.....	35
Figure 12: AOD at 550nm in IFS model simulations for April 2011 - February 2016 against daily matching Aeronet NRT level 1.5 and level 2.0 data a) Modified normalized mean bias (MNMB); o-suite (thick red curve); o-suite at last forecast day (light red curve); Control (blue dashed); Control at last forecast day (light blue dashed); o-suite but evaluated against quality assured Aeronet level 2.0 data (orange dashed); b) Corresponding correlation coefficient	37

List of Tables

Table 1 - The LSA SAF Set of Products and respective sensors and platforms. The table covers both existing and future EUMETSAT satellites, and therefore refers to operational products and development activities.	9
Table 2 - Product Requirements for ETAL, in terms of area coverage, resolution and accuracy.	12
Table 3 - Serie of Meteosat satellites considered for product achievement.	12
Table 4 - Coefficients for the parameterization of the TOC reflectance factor uncertainty estimates.....	23
Table 5 - Narrow- to broad-band conversion coefficients for the AVHRR channels (van Leeuwen and Roujean, 2002).....	29
Table 6 - Narrow- to broad-band conversion coefficients for pixels flagged as snow-covered for AVHRR calculated with tools developed by Samain (2005)..	30

1 The EUMETSAT SAF on Land Surface Analysis

The Satellite Application Facility (SAF) on Land Surface Analysis (LSA) is part of the SAF Network, a set of specialised development and processing centres, serving as EUMETSAT (European organization for the Exploitation of Meteorological Satellites) distributed Applications Ground Segment. The SAF network complements the product-oriented activities at the EUMETSAT Central Facility in Darmstadt. The main purpose of the LSA SAF is to take full advantage of remotely sensed data, particularly those available from EUMETSAT sensors, to measure land surface variables, which will find primarily applications in meteorology (<http://landsaf.ipma.pt/>).

The EUMETSAT Polar System (EPS) is Europe's first polar orbiting operational meteorological satellite and the European contribution to a joint polar system with the U.S. EUMETSAT will have the operational responsibility for the "morning orbit" with Meteorological-Operational (Metop) satellites, the first of which was successfully launched on October 19, 2006. Despite the wide range of sensors on-board Metop (<http://www.eumetsat.int/>), most LSA SAF parameters make use of the observations issued from the Advanced Very High Resolution Radiometer (AVHRR) instrument. AVHRR offers capability to observe the whole globe every day at 1 km resolution (at nadir), in the visible and infrared bands of the electromagnetic spectrum.

Several studies have stressed the role of land surface processes on weather forecasting and climate modelling (e.g., *Dickinson et al., 1983; Mitchell et al., 2004; Ferranti and Viterbo, 2006*). The LSA SAF has been especially designed to serve the needs of the meteorological community, particularly Numerical Weather Prediction (NWP). However, there is no doubt that the LSA SAF addresses a much broader community, which includes users from:

- Weather forecasting and climate modelling, requiring detailed information on the nature and properties of land.
- Environmental management and land use, needing information on land cover type and land cover changes (e.g. provided by biophysical parameters or thermal characteristics).
- Agricultural and Forestry applications, requiring information on incoming/outgoing radiation and vegetation properties.
- Renewable energy resources assessment, particularly biomass, depending on biophysical parameters, and solar energy.
- Natural hazards management, requiring frequent observations of terrestrial surfaces in both the solar and thermal bands.
- Climatological applications and climate change detection, requiring long and homogeneous time-series.

Table 1 - The LSA SAF Set of Products and respective sensors and platforms. The table covers both existing and future EUMETSAT satellites, and therefore refers to operational products and development activities.

Product Family	Product Group	Sensors/Platforms
Radiation	Land Surface Temperature (LST)	SEVIRI/MSG, AVHRR/Metop, FCI/MTG, VII/EPS-SG
	Land Surface Emissivity (EM)	SEVIRI/MSG, FCI/MTG (internal product for other sensors)
	Land Surface Albedo (AL)	SEVIRI/MSG, AVHRR/Metop, FCI/MTG, VII/EPS-SG, 3MI/EPS-SG
	Down-welling Short-wave Fluxes (DSSF)	SEVIRI/MSG, FCI/MTG
	Down-welling Long-wave Fluxes (DSLFL)	SEVIRI/MSG, FCI/MTG
Vegetation	Normalized Difference Vegetation Index (NDVI)	AVHRR/Metop, VII/EPS-SG
	Fraction of Vegetation Cover (FVC)	SEVIRI/MSG, AVHRR/Metop, FCI/MTG, VII/EPS-SG, 3MI/EPS-SG
	Leaf Area Index (LAI)	SEVIRI/MSG, AVHRR/Metop, FCI/MTG, VII/EPS-SG, 3MI/EPS-SG
	Fraction of Absorbed Photosynthetically Active Radiation (FAPAR)	SEVIRI/MSG, AVHRR/Metop, FCI/MTG, VII/EPS-SG, 3MI/EPS-SG
	Gross Primary Production (GPP)	SEVIRI/MSG, FCI/MTG
	Canopy Water Content (CWC)	AVHRR/Metop, VII/EPS-SG
Energy Fluxes	Evapotranspiration (ET)	SEVIRI/MSG, FCI/MTG
	Reference Evapotranspiration (ET0)	SEVIRI/MSG, FCI/MTG
	Surface Energy Fluxes: Latent and Sensible (LE&H)	SEVIRI/MSG, FCI/MTG
Wild Fires	Fire Detection and Monitoring (FD&M)	SEVIRI/MSG
	Fire Radiative Power	SEVIRI/MSG, FCI/MTG, VII/EPS-SG
	Fire Radiative Energy and Emissions (FRE)	SEVIRI/MSG, FCI/MTG, VII/EPS-SG
	Fire Risk Map (FRM)	SEVIRI/MSG, FCI/MTG
	Burnt Area (BA)	AVHRR/Metop, VII/EPS-SG

The LSA SAF products (Table 1) are based on level 1.5 SEVIRI/Meteosat and/or level 1b Metop data. Forecasts provided by the European Centre for Medium-range Weather Forecasts (ECMWF) are also used as ancillary data for atmospheric correction.

Metop derived parameters are currently available at level 3 full globe in sinusoidal projection, centred at (0°N, 0°W), with a resolution of 0.01° by 0.01°, one file for daytime and another for nighttime observations.

The LSA SAF system is located at IPMA (Portugal) and VITO (Belgium) and has been designed to generate, to archive, and to disseminate the operational products. LSA SAF Land Surface Temperature products are fully centralized at IPMA. The monitoring and quality control of the operational products is performed automatically by the LSA SAF software, which provides quality information to be distributed with the products.

The LSA SAF products are currently available from LSA SAF website (<http://landsaf.ipma.pt>) that contains real time examples of the products as well as updated information.

2 Introduction

Land surface albedo (AL) is a key variable for characterizing the energy balance in the coupled surface-atmosphere system. It represents a crucial variable for soil-vegetation-atmosphere transfer modeling. As a matter of fact, land surface albedo quantifies the fraction of energy reflected by the surface of the Earth. As a corollary, AL also determines the fraction of energy absorbed by the surface and transformed into heat or latent energy but also into photosynthesis for the PAR range.

Owing to strong feedback effects, the knowledge of surface albedo is also paramount for determining atmospheric conditions in the boundary layer. Numerical Weather Prediction (NWP) models are in constant evolution and are becoming eager to ingest a surface albedo product following an assimilation procedure (*Cedilnik et al. 2012*). On the other hand, this pushes the product developers to increase the accuracy assessment of AL products in terms of the spatial and temporal resolutions. On longer timescales, past studies pointed out in using Global Circulation Models the sensitivity of climate with respect to changes in surface albedo.

The largest surface albedo changes are caused by snow fall merely, if one excepts hazards. Snow characteristics and duration of snow cover have a direct impact on the environmental system. The seasonal monitoring of snow therefore is an important subject for NWP, climate studies, and hydrology. Snow albedo varies with environmental conditions, land cover, and snow metamorphism. The objectives of the delivered AL product is to capture the albedo changes occurring on short timescales, with obviously better perspectives for GEO than for LEO satellites.

The most relevant AL quantity for the energy budget refers to the total short-wave broad-band interval comprising the visible and near infrared wavelength ranges where the solar down-welling radiation dominates. In more refined models the albedo values in the visible and near infrared broad-band ranges may also be exploited separately. LSA SAF algorithm also delivers reflectance factor values and the spectral albedo in the satellite instrument channels upon request. In addition to serving as an intermediate product for deriving the broad-band albedo quantities, the spectral estimates contain a wealth of information about the physical state of the surface. This information can be used for a variety of purposes such as vegetation

monitoring and land cover classification. In turn, this also constitute important elements for setting up adequate surface modeling schemes (*Carrer et al. 2012*).

A well-established approach for operational albedo determination is based on semi-empirical BRDF (Bidirectional Reflectance Distribution Function) kernel models which have received a great deal of attention and effort from the optical remote sensing community in the last decades (e.g., *Roujean et al., 1992; Barnsley et al., 1994; Wanner et al., 1995; Strahler, 1994; and Hu et al., 1997*). The approach is based on a decomposition of the bi-directional reflectance factor into a number of kernel functions which are associated to dominant light scattering processes. For example, geometric and volumetric effects, separation between soil and vegetation contributions, or the conjunction between media which are optically thick and thin (*Lucht and Roujean, 2000*). Both in situ measurements and numerical experiments have supported this assumption and the use of kernel-based models is nowadays widely accepted as this category of models yields a pragmatic and cost-effective solution to the problem of BRDF inversion. For a number of space-borne sensors of the current generation of multi-angular systems the kernel-based approach was adopted for the development of albedo products. These include POLDER, SeaWiFS, VEGETATION, and MODIS (e.g., *Leroy et al., 1997; Justice et al., 1998; Wanner et al., 1997; Strahler et al., 1999*). On the other hand, different parametrized models and a simultaneous modeling of atmosphere and surface properties were considered for MISR (*Diner et al., 1998*) and Meteosat (*Pinty et al., 2000a-b*). The common feature of these algorithms is the correction and exploitation of the variations in sun-sensor geometry that occur as a function of satellite orbit, sensor design, geographical position of the target, and time of the year. There are also purely observation-based methods dealing with BRDF description and inversion, e.g. the angular binnig method used for the generation of the GLASS albedo dataset (<http://glcf.umd.edu/data/abd/>).

The AL product of the LSA-SAF is for time being produced from data acquired by the Spinning Enhanced Visible and Infrared Imager (SEVIRI) radiometer embarked on MSG. The AL product from the Advanced Very High Resolution Radiometer (AVHRR) aboard the series of Metop satellites is a pre-operational product for the time being. Forecasts provided by the European Center for Medium-range Weather Forecasts (ECMWF) are used as ancillary data for the atmospheric correction prior to the estimation of the AL products.

One major issue impacting the AL precision is due to aerosols. An appropriate knowledge is suitable both in time and space. As the context is operational here, an aerosol correction must be equally performed anytime. For this reason, CAMS products from Copernicus will be used in departing from a climatology-based approach.

The present document is one of the product manuals dedicated to LSA SAF users. The algorithm theoretical basis of the land surface albedo generated by the LSA SAF are described in the following sections. The characteristics of the AL products derived from AVHRR and provided by the LSA SAF are described in Table 2. Further details on the AL product requirements may be found in the Product Requirements

Document (PRD) and the Product User Manual (PUM) which are available on the LSA SAF website.

Table 2 - Product Requirements for ETAL, in terms of area coverage, resolution and accuracy.

Product Name	Product Identifier	Coverage	Resolution		Accuracy		
			Temporal	Spatial	Threshold	Target	Optimal
ETAL (AL AVHRR)	LSA-103	Global	10-day	0.01° x 0.01°	AL>0.15: 20% AL<0.15: 0.03	AL>0.15 15% AL<0.15: 0.0225	AL>0.15: 5% AL<0.15: 0.01

The Table 3 below detailed the evolution of the MetOP platforms considered in the frame of the LSA SAF project and the changes operated.

Table 3 – Series of MetOP satellites considered for product achievement.

	MetOP-A	MetOP-B	MetOP-C
Period	19/10/2006	17/09/2012	End of 2017
Operated changes	Calibration Band factors	Calibration Band factors	Calibration Band factors

3 Theoretical framework

The spectral albedo of a plane surface is defined as the ratio between the hemispherical integrals of the up-welling (reflected) spectral radiance $L^\uparrow(\lambda, \theta_{out}, \varphi_{out})$ and the down-welling spectral radiance $L^\downarrow(\lambda, \theta_{in}, \varphi_{in})$ weighted by the cosine of the angle between the respective reference direction and the surface normal:

$$a(\lambda) := \frac{\int L^\uparrow(\lambda, \theta_{out}, \varphi_{out}) \cos \theta_{out} d\Omega_{out}}{\int_{2\pi} L^\downarrow(\lambda, \theta_{in}, \varphi_{in}) \cos \theta_{in} d\Omega_{in}}, \quad (1)$$

where $d\Omega_{out} = \sin \theta_{out} d\theta_{out} d\varphi_{out}$ and $d\Omega_{in} = \sin \theta_{in} d\theta_{in} d\varphi_{in}$. In other words, the term in the denominator defines the spectral solar irradiance $E^\downarrow(\lambda)$. By introducing the bi-directional reflectance factor R , the up-welling radiance distribution can be expressed in terms of the down-welling radiation as

$$L^\uparrow(\lambda, \theta_{out}, \varphi_{out}) = \frac{1}{\pi} \int_{2\pi} R(\lambda, \theta_{out}, \varphi_{out}, \theta_{in}, \varphi_{in}) L^\downarrow(\lambda, \theta_{in}, \varphi_{in}) \cos \theta_{in} d\Omega_{in}, \quad (2)$$

and Equation (1) becomes

$$a(\lambda) = \frac{\frac{1}{\pi} \int_{2\pi} \int_{2\pi} R(\lambda, \theta_{out}, \varphi_{out}, \theta_{in}, \varphi_{in}) L^\downarrow(\lambda, \theta_{in}, \varphi_{in}) \cos \theta_{in} \cos \theta_{out} d\Omega_{in} d\Omega_{out}}{E^\downarrow(\lambda)}. \quad (3)$$

It can be seen from the equation (3) that the spectral albedo of non-Lambertian surfaces generally depends on the angular distribution of the incident radiation, which in turn depends on the concentration and properties of scattering agents (e.g., aerosols) in the atmosphere and, in particular, on the presence of clouds. Therefore the spectral albedo is not a true surface property but rather a characteristic of the coupled surface-atmosphere system.

In the idealized case of totally direct illumination at incidence angles $(\theta_{dh}, \varphi_{dh})$, the down-welling radiance is given by $L^\downarrow(\lambda, \theta_{in}, \varphi_{in}) = (\sin \theta_{dh})^{-1} \delta(\theta_{in} - \theta_{dh}, \varphi_{in} - \varphi_{dh}) E_0(\lambda)$, which results in $E^\downarrow(\lambda) = E_0(\lambda) \cos \theta_{dh}$ and

$$L^\uparrow(\lambda, \theta_{out}, \varphi_{out}; \theta_{dh}, \varphi_{dh}) = \frac{1}{\pi} R(\lambda, \theta_{out}, \varphi_{out}, \theta_{dh}, \varphi_{dh}) E_0(\lambda) \cos \theta_{dh}. \quad (4)$$

By inserting these expressions into Equation (3) we obtain the spectral directional-hemispherical (or “black-sky”) albedo $a^{dh}(\lambda; \theta_{dh}, \varphi_{dh})$:

$$a^{dh}(\lambda; \theta_{dh}, \varphi_{dh}) = \frac{1}{\pi} \int_{2\pi} R(\lambda, \theta_{out}, \varphi_{out}, \theta_{dh}, \varphi_{dh}) \cos \theta_{out} d\Omega_{out}. \quad (5)$$

On the other hand, in the case of completely diffuse illumination the down-welling radiance $L^\downarrow(\lambda, \theta_{in}, \varphi_{in}) = L_0(\lambda)$ is constant and the solar irradiance becomes $E^\downarrow(\lambda) = \pi L_0(\lambda)$. By inserting these terms into Equation (3) and after making use of

Equation (5) the spectral bi-hemispherical (or “white-sky”) albedo $a^{bh}(\lambda)$ can be written as:

$$a^{bh}(\lambda) = \frac{1}{\pi} \int_{2\pi} a^{dh}(\lambda; \theta_{in}, \varphi_{in}) \cos \theta_{in} d\Omega_{in} . \quad (6)$$

These two quantities are true surface properties and correspond to the limiting cases of point source ($a^{dh}(\lambda; \theta_{dh}, \varphi_{dh})$) and completely diffuse illumination ($a^{bh}(\lambda)$). For partially diffuse illumination the actually occurring spectral albedo value may be approximated as a linear combination of the limiting cases

$$a(\lambda) \approx [1 - f_{diffuse}(\lambda)] a^{dh}(\lambda; \theta_s, \varphi_s) + f_{diffuse}(\lambda) a^{bh}(\lambda) , \quad (7)$$

where $f_{diffuse}$ denotes the fraction of diffuse radiation and (θ_s, φ_s) the solar direction.

For many applications the quantity of interest is not the spectral, or narrow-band, but rather the broad-band albedo which is defined as the ratio of up-welling to down-welling radiation fluxes in a given wavelength interval $[\lambda_1, \lambda_2]$:

$$a_{[\lambda_1, \lambda_2]} := \frac{F_{[\lambda_1, \lambda_2]}^{\uparrow}}{F_{[\lambda_1, \lambda_2]}^{\downarrow}} = \frac{\int_{\lambda_1}^{\lambda_2} \int_{2\pi} L^{\uparrow}(\lambda, \theta_{out}, \varphi_{out}) \cos \theta_{out} d\Omega_{out} d\lambda}{\int_{\lambda_1}^{\lambda_2} \int_{2\pi} L^{\downarrow}(\lambda, \theta_{in}, \varphi_{in}) \cos \theta_{in} d\Omega_{in} d\lambda} . \quad (8)$$

In analogy to Equation (3) it can be expressed in terms of the bi-directional reflectance factor as

$$a(\lambda) = \frac{\frac{1}{\pi} \int_{\lambda_1}^{\lambda_2} \int_{2\pi} \int_{2\pi} R(\lambda, \theta_{out}, \varphi_{out}, \theta_{in}, \varphi_{in}) L^{\downarrow}(\lambda, \theta_{in}, \varphi_{in}) \cos \theta_{in} \cos \theta_{out} d\Omega_{in} d\Omega_{out} d\lambda}{F_{[\lambda_1, \lambda_2]}^{\downarrow}} . \quad (9)$$

In this case the directional-hemispherical broad-band albedo

$$a_{[\lambda_1, \lambda_2]}^{dh}(\theta_{dh}, \varphi_{dh}) = \frac{\int_{\lambda_1}^{\lambda_2} a^{dh}(\lambda; \theta_{dh}, \varphi_{dh}) E^{\downarrow}(\lambda) d\lambda}{\int_{\lambda_1}^{\lambda_2} E^{\downarrow}(\lambda) d\lambda} , \quad (10)$$

and the bi-hemispherical broad-band albedo

$$a_{[\lambda_1, \lambda_2]}^{bh} = \frac{\int_{\lambda_1}^{\lambda_2} a^{bh}(\lambda) E^\downarrow(\lambda) d\lambda}{\int_{\lambda_1}^{\lambda_2} E^\downarrow(\lambda) d\lambda}, \quad (11)$$

can be written as integrals of the respective spectral quantities weighted by the spectral irradiance. The corresponding broad-band albedo values are not pure surface properties since the wavelength dependence of the spectral irradiance $E(\lambda)$ appearing as a weight factor in their definition may vary as a function of the atmospheric composition. In analogy to Equation (7) the broad-band albedo for partially diffuse illumination conditions may be expressed as a weighted average of $a_{[\lambda_1, \lambda_2]}^{dh}(\theta_s, \varphi_s)$ and $a_{[\lambda_1, \lambda_2]}^{bh}$.

4 Algorithm description

4.1 Overview

Satellite observations provide TOA radiance measurements for certain configurations of illumination and observation geometry. The calculation of surface albedo according to the equations above requires the knowledge of the complete BRDF of the surface. To obtain an estimate of this quantity it is necessary to solve the radiative transfer problem in the coupled surface-atmosphere system. Herein, a simplified consolidated approach is adopted. In a first step an atmospheric correction is performed in order to derive top-of-canopy (TOC) reflectance values corresponding to the occurring angular observation configurations. In a second step, the coefficients of a semi-empirical kernel-based reflectance model are adjusted against a set of measurements. This delivers an estimate of the complete angular dependence of the bi-directional reflectance factor R_β in the spectral channel β of the measuring instrument:

$$R_\beta(\theta_{out}, \theta_{in}, \varphi) = \mathbf{k}_\beta \mathbf{f}(\theta_{out}, \theta_{in}, \varphi). \quad (12)$$

Here $\mathbf{k}_\beta = (k_{0\beta}, k_{1\beta}, k_{2\beta}, \dots)^T$ and $\mathbf{f} = (f_0, f_1, f_2, \dots)^T$ represent vectors formed by the retrieved model parameters $k_{i\beta}$ and the kernel functions f_i , respectively. The individual azimuth angles were replaced by the relative azimuth angle φ between the directions of incoming and outgoing light paths. This is possible without restriction of generality as long as the surface is considered as spatially isotropic.

The proposed algorithm consists in calculating the “black-sky” a_β^{dh} and “white-sky” a_β^{bh} albedos (BSA & WSA) defined by integrals (5) and (6) in all instrument channels β by using the coefficients \mathbf{k}_β provided by the directional reflectance model inversion. The narrow-band albedo values serve as an approximation to the spectral albedo at the central band wavelength λ_β . Furthermore broad-band albedo values a_γ^{dh} and a_γ^{bh} corresponding to suitable intervals $\gamma = [\lambda_1, \lambda_2]$ are derived from the

spectral estimates by employing appropriate approximations to the integrals (10) and (11).

The operational processing scheme of the LSA SAF albedo algorithm is depicted in the flow chart of Figure 1 and comprises the following four successive steps:

1. First the measured top-of-atmosphere (TOA) radiances delivered by the satellite instrument are corrected for atmospheric effects in order to convert them into the corresponding TOC reflectance values.
2. The spectral TOC reflectance values then serve as input quantities for the inversion of a linear kernel-driven BRDF model, which allows us to take into account the angular dependence of the reflectance factor.
3. Spectral albedo values in the instrument channels are determined from the angular integrals of the model functions with the retrieved parameter values.
4. Finally, a narrow to broad-band conversion is performed with a linear regression formula.

Technically speaking the processing chain comprises two distinct modules:

- a module for atmospheric correction
- a module for model inversion and directional and spectral integration.

The atmospheric correction module is applied separately on each SEVIRI or AVHRR image available at intervals of 15 minutes or 1 day directly after acquisition. Note that the AVHRR data used are from only one Metop (Metop-B for the time being). The module for ETAL product computation operates on a set of images in TOC reflectance units collected during several successive day. By using the previous inversion result as a priori information, a recursive temporal composition of the information over a longer time period can be achieved in order to guarantee the coherence and spatial completeness of the product. This will be described further in this document.

It is worth mentioning here that the BRDF model retained obeys to the Helmholtz principle of reciprocity, which means that the model will remain still valid by exchanging the directions of illumination and scanning. Viewing angles are varying and the solar angle remains relatively constant for EPS/AVHRR.

A concern is the incoming diffuse radiation. So far, only BRDF model is inverted against set of observations assumed to be clear from sunrise to sunset. At grazing illumination, the diffuse component will dominate and BSA will have to be introduced in the BRDF model. The weight of this is the diffuse fraction which will be derived from aerosol load derived from CAMS, either a climatology or near real time products. This is in test and not implemented yet.

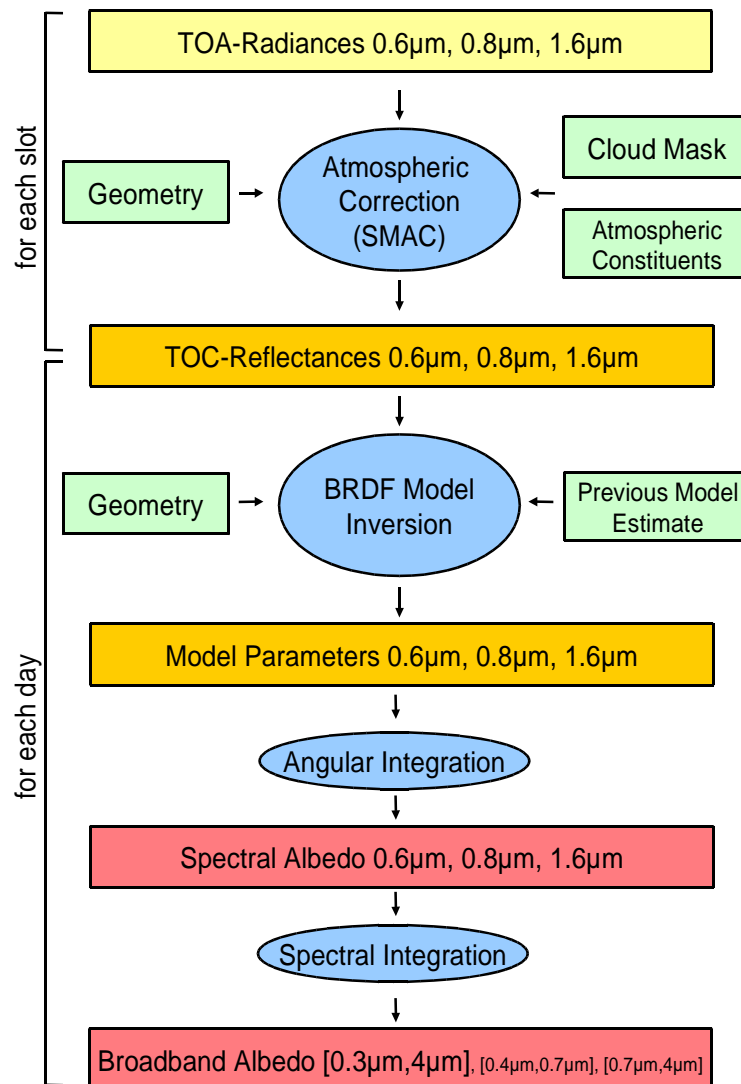


Figure 1: Flow chart of the algorithm for atmospheric correction, BRDF model inversion, and albedo determination.

4.2 Atmospheric correction

The LSA SAF operational system provides TOA radiances as well as all auxiliary information needed to perform atmospheric correction at the temporal resolution of the image acquisition and the spatial resolution of the AVHRR instrument. The required quantities include the illumination and observation angles, a land/water-mask, the cloud-mask product (CMA) generated with software components developed by the Nowcasting-SAF, surface pressure information obtained from the ECMWF numerical weather prediction model combined with the use of a digital elevation model, column water vapor and ozone content from ECMWF, and aerosol climatology from CAMS (see Section 4.6).

The measurements of the TOA radiance \hat{L}_β in the spectral channels of the AVHRR instrument are first converted to TOA reflectance factor values:

$$\hat{R}_\beta = \frac{\hat{L}_\beta}{B_\beta \nu(t) \cos \theta_s} \quad (13)$$

The band factor B_β depends on the solar spectral irradiance and the spectral sensitivity of the respective channel (Derrien, 2002). The numerical values currently used for MetopB/AVHRR are for the 0.6 μm , 0.8 μm , and 1.6 μm channels, respectively, 44.6589, 77.9859 and 4.1699 (in $\text{W}/\text{m}^2/\text{sr}$).

The factor $\nu(t)$ takes into account the varying distance of the Sun as a function of the day t of the year.

The atmospheric correction module is based on SMAC, the Simplified Method for the Atmospheric Correction of satellite measurements in the solar spectrum (Rahman and Dedieu, 1994). TOC reflectance values R_β are calculated from the TOA values \hat{R}_β as

$$R_\beta = \frac{\tilde{R}_\beta}{1 + \tilde{R}_\beta S_\beta} \quad \text{with} \quad \tilde{R}_\beta = \frac{\hat{R}_\beta - T_\beta^{\text{gas}} R_\beta^{\text{atm}}}{T_\beta^{\text{gas}} T_\beta(\theta_s) T_\beta(\theta_v)} \quad (14)$$

where S_β is the spherical albedo of the atmosphere, T_β^{gas} is the total gaseous transmission, R_β^{atm} the ‘‘atmospheric reflectance’’, and $T_\beta(\theta_s)$ and $T_\beta(\theta_v)$ ‘‘atmospheric diffuse transmittance’’ in the solar and viewing directions as it is defined by Rahman and Dedieu (1994). These quantities, which characterize the atmospheric absorption and scattering processes, are calculated from information about the atmospheric constituents by means of parameterizations with simple analytic functions whose coefficients depend on the spectral response of the respective channel considered. For our application the relevant coefficients corresponding to the AVHRR 0.6 μm , 0.8 μm , and 1.6 μm channels were provided by Berthelot (2001). A continental aerosol type is considered for all situations.

The aerosol correction makes use of the AOD at 550nm from Copernicus Atmosphere Monitoring Service (CAMS). This initiative disseminates in near-real time (NRT) conditions the aerosol content and other atmospheric products based on a transport model for atmospheric particles with dedicated identification of sources and sinks. So far, a CAMS climatology is used to perform an aerosol correction on spectral AVHRR reflectance values further used to generate the ETAL product. (see Section 4.6) Worth emphasizing that there is not limitation for the AOD value.

The TOC reflectance values for the three used channels are determined for all AVHRR scenes and are available as an internal product in the LSA SAF system. In the following methodological discussion we assume that all atmospheric effects are correctly accounted for and we consider the obtained results as true bi-directional reflectance factor values. In practice inaccurate knowledge of the atmospheric composition as well as simplifications in the correction approach can introduce random as well as systematic uncertainties. This point is illustrated in the Validation Report (VR) document.

4.3 Albedo calculation

4.3.1 Inversion method

The atmospheric correction carried out by SMAC provides a set of n reflectance measurements $R_{j\beta}$ ($j=1, \dots, n$) in different spectral channels β given at irregularly spaced time points t_j and varying discrete values of the view θ_{vj} and solar zenith angles θ_{sj} (see Figure 2 for an example case). In the algorithm a linear kernel-based directional reflectance model of the form shown in Equation (12) is applied separately to each spectral band. In the following the index β referring to the channel is omitted for simplicity.

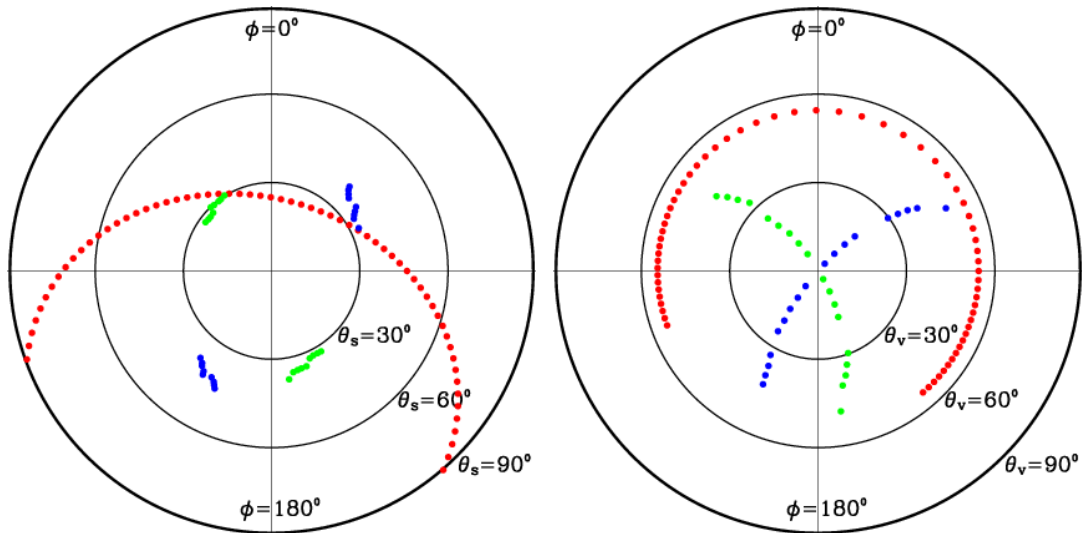


Figure 2: Illumination (left) and observation (right) geometries corresponding to a geographical location of [47° 47' N, 10° 37' E] and an observation period between the days of year 150 and 170. The relative azimuth angle ϕ is identical for the two graphs. The convention was chosen such that the top of the graphs ($\phi = 0^\circ$) corresponds to the back scattering regime. The colors of the dots denote observations taken by different sensors as follows: Red: SEVIRI/MSG, Green: AVHRR/METOP, Blue: AVHRR/NOAA.

The available TOC reflectance measurements provide the following system of n linear equations

$$R_j(\theta_{vj}, \theta_{sj}, \varphi_j) = \sum_{i=0}^{m-1} k_i f_i(\theta_{vj}, \theta_{sj}, \varphi_j) \quad (j=1, \dots, n), \quad (15)$$

for constraining the m model parameters k_i ($i=0, \dots, m-1$). Introducing the vectors $\mathbf{k} = (k_0, k_1, \dots, k_{m-1})^T$ and $\mathbf{R} = (R_1, R_2, \dots, R_n)^T$, and the (n, m) -matrix \mathbf{F} with the elements $F_{ji} = f_i(\theta_{vj}, \theta_{sj}, \varphi_j)$, allows us to rewrite the equation system in its matrix form:

$$\mathbf{R} = \mathbf{F} \mathbf{k} . \quad (16)$$

In general the number of available observations is larger than the number of unknown parameters and thus no exact solution for \mathbf{k} exists. However, the observed reflectance is affected by measurement errors and therefore it is convenient to search for the best solution in a statistical sense and to quantify the uncertainties of the retrieved parameter estimates. In this case it may turn out that a considerably larger number of observations than parameters are required in order to reasonably constrain the parameter values.

The uncertainties of the individual reflectance factor measurements R_j are quantified by means of weight factors w_j , which are related to the inverse of the standard “1-sigma” uncertainty estimates $\sigma[R_j]$. We introduce the scaled reflectance vector \mathbf{b} with the elements $b_j = R_j w_j$ and the “design matrix” \mathbf{A} with the elements $A_{ji} = F_{ji} w_j$ (see e.g., Press et al., 1995). The linear least squares solution to the inversion problem in Equation (12) can be found by solving the “normal equations”

$$(\mathbf{A}^T \mathbf{A}) \mathbf{k} = \mathbf{A}^T \mathbf{b} , \quad (17)$$

for the parameters \mathbf{k} . The uncertainty covariance matrix of the retrieved model parameters is given by

$$\mathbf{C}_k = (\mathbf{A}^T \mathbf{A})^{-1} . \quad (18)$$

The diagonal elements C_{jj} of this matrix represent the variance $\sigma^2[k_j]$ of the respective parameters k_j . The covariance between k_i and k_j is given by the off-diagonal elements C_{ij} .

If the matrix $\mathbf{A}^T \mathbf{A}$ is far from being singular, the solution can be found by multiplying Equation (18) “from the left” by the covariance matrix \mathbf{C}_k . In most of the cases this is feasible with a sufficient numerical accuracy. However, if a very small number of measurements are available and the angular configuration is unfavorable (which is more likely to occur for geostationary satellite observations) the application of robust techniques involving singular value decomposition (SVD) and/or QR-decomposition is necessary to limit the effects of numerical errors when calculating the parameter estimates $\mathbf{k} = (k_0, k_1, k_2)^T$ and the uncertainty covariance matrix \mathbf{C}_k .

To improve the result of the parameter estimation it can be useful to add constraints on the parameters themselves in the inversion of the linear model (e.g., Li et al., 2001; Hagolle et al. 2004; a related approach was also adopted by Pokrovsky et al. 2003). In the following we consider independent and uncorrelated a priori information on the parameters expressed in terms of the first and second moments (average and standard deviation, respectively) of their a priori probability distribution function, that is, an estimate of the form

$$k_i = k_{i \text{ ap}} \pm \sigma_{\text{ap}}[k_i] . \quad (19)$$

To simplify the notation let us consider an example with $m = 3$ and an additional constraint for the two parameters k_1 and k_2 . In this case adding the constraint of expression (19) to the equation system 18 corresponds to extending the (n, m) -matrix \mathbf{A} to the $(n + 2, m)$ -matrix

$$\mathbf{A}' = \begin{pmatrix} \mathbf{A} & & \\ 0 & \sigma_{\text{ap}}^{-1}[k_1] & 0 \\ 0 & 0 & \sigma_{\text{ap}}^{-1}[k_2] \end{pmatrix}, \quad (20)$$

and to extending the vector \mathbf{b} to $\mathbf{b}' = (b_1, \dots, b_n, k_{1 \text{ ap}} \sigma_{\text{ap}}^{-1}[k_1], k_{2 \text{ ap}} \sigma_{\text{ap}}^{-1}[k_2])^T$. The linear least squares solution with a priori information is then obtained in the same way as above by solving the normal equations.

More generally, taking into account a multivariate Gaussian a priori probability distribution function for the parameters quantified by its first and second moments corresponds to re-writing Equations (18) and (19) in the form

$$(\mathbf{A}^T \mathbf{A} + \mathbf{C}_{\text{ap}}^{-1}) \mathbf{k} = \mathbf{A}^T \mathbf{b} + \mathbf{C}_{\text{ap}}^{-1} \mathbf{k}_{\text{ap}}, \quad (21)$$

and

$$\mathbf{C}_{\mathbf{k}} = (\mathbf{A}^T \mathbf{A} + \mathbf{C}_{\text{ap}}^{-1})^{-1}, \quad (22)$$

with $\mathbf{k}_{\text{ap}} = (k_{0 \text{ ap}}, \dots, k_{m-1 \text{ ap}})^T$ and the covariance matrix \mathbf{C}_{ap} . For uncorrelated a priori information on the parameters the matrix $\mathbf{C}_{\text{ap}} = \text{diag}(\sigma_{\text{ap}}^2[k_0], \dots, \sigma_{\text{ap}}^2[k_m])$ is diagonal. Absence of a priori information on a given parameter – like it is the case for k_0 in the example case leading to the expression – corresponds to $\sigma_{\text{ap}}[k_i] \rightarrow \infty$ and $\sigma_{\text{ap}}^{-2}[k_i] \rightarrow 0$.

By adding constraints on $m - 1$ model parameters, the inversion can be carried out with a minimum number of one available observation. In addition, the constraints on the parameters reduce the condition number of the involved matrix and mitigate potential numerical problems. In practice we therefore add a regularization term corresponding to $k_1 = 0.03 \pm 0.05$ and $k_2 = 0.3 \pm 0.5$ which does not lead to a noticeable prejudice in the inversion result.

4.3.2 Surface BRDF model

In the following we restrict the discussion to a model with three parameters of the following form:

$$R(\theta_{out}, \theta_{in}, \varphi) = k_0 + k_1 f_1(\theta_{out}, \theta_{in}, \varphi) + k_2 f_2(\theta_{out}, \theta_{in}, \varphi). \quad (23)$$

In the LSA SAF AL algorithm while k_0 quantifies an isotropic contribution to the reflectance factor ($f_0=1$), functions f_1 and f_2 represent the angular distribution related to geometric and volumetric surface scattering processes, respectively. Roujean et al. (1992) suggest the following analytical expressions:

$$f_1(\theta_{out}, \theta_{in}, \varphi) = \frac{1}{2\pi} [(\pi - \varphi) \cos \varphi + \sin \varphi] \tan \theta_{out} \tan \theta_{in} - \frac{1}{\pi} (\tan \theta_{out} + \tan \theta_{in} + \sqrt{\tan^2 \theta_{out} + \tan^2 \theta_{in} - 2 \tan \theta_{out} \tan \theta_{in} \cos \varphi}), \quad (24)$$

(for $\varphi \in [0, \pi]$) and

$$f_2(\theta_{out}, \theta_{in}, \varphi) = \frac{4}{3\pi} \frac{1}{\cos \theta_{out} + \cos \theta_{in}} [(\frac{\pi}{2} - \zeta) \cos \zeta + \sin \zeta] - \frac{1}{3}, \quad (25)$$

with the phase angle

$$\zeta = \arccos[\cos \theta_{out} \cos \theta_{in} + \sin \theta_{out} \sin \theta_{in} \cos \varphi]. \quad (26)$$

Figure 3 depicts the dependence of these kernel functions on the zenith angle of the reflected light-ray for different illumination directions.

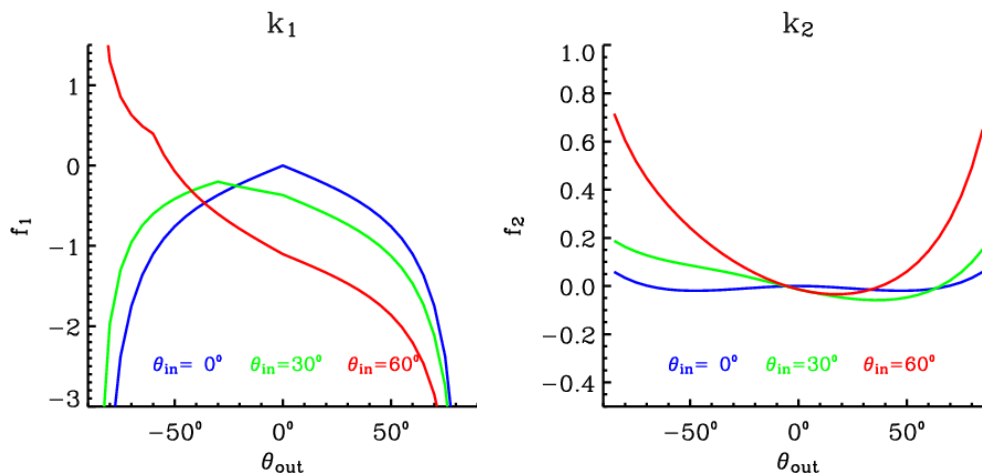


Figure 3: Angular dependence of the geometric (left) and volumetric (right) scattering kernels of the reflectance model introduced by Roujean et al. (1992). Negative zenith angle values correspond to the back scattering direction (relative azimuth angle $\varphi = 0^\circ$) and positive zenith angle values to the forward scattering direction ($\varphi = 180^\circ$).

4.3.3 Weighting of measurements

The matrix $F_{ji} = f_i(\theta_{vj}, \theta_{sj}, \varphi_j)$ is calculated knowing the angular configuration of each measurement point t_j . In order to determine the scaled reflectance vector \mathbf{b} and the design matrix \mathbf{A} it is necessary to specify the weight factors w_j . We choose an expression of the form

$$w_j = w_\theta(\theta_{vj}, \theta_{sj}) w_t(t_j), \quad (27)$$

which simultaneously characterizes the angular as well as the temporal dependence of the weight attributed to each measurement point. In the current configuration of the algorithm the temporal weight function

$$w_t(t_j) = 1, \quad (28)$$

is kept constant since reflectance measurements for direct inversion are accumulated over one day and the temporal composition of the daily observations is handled recursively as described in Section 4.3.5. The angular component

$$w_\theta(\theta_{vj}, \theta_{sj}) = \frac{1}{\sigma[R_j(\theta_{vj}, \theta_{sj})]}, \quad (29)$$

of the weight function is conveniently defined as the inverse of the estimated uncertainty of the reflectance measurements whose directional dependence is assumed to be a linear function of the relative air-mass $\eta(\theta_{vj}, \theta_{sj})$:

$$\sigma[R_j(\theta_{vj}, \theta_{sj})] = \sigma[R_j(\theta_v=0^\circ, \theta_s=0^\circ)] \eta(\theta_{vj}, \theta_{sj}). \quad (30)$$

Estimates for the values of the reference uncertainties $\sigma[R_j(\theta_v=0^\circ, \theta_s=0^\circ)]$ at normalized geometry were obtained from a statistical analysis of atmospherically corrected AVHRR scenes and are expressed as a linear function of the reflectance factor value

$$\sigma[R_j(\theta_v=0^\circ, \theta_s=0^\circ)] = c_1 + c_2 R_j, \quad (31)$$

with coefficients for the three spectral bands as specified in Table 4. A lower limit of 0.005 and an upper limit of 0.05 are imposed to this quantity in order to avoid extreme values for reflectance outliers. A description of the method applied for obtaining the uncertainty estimates in a similar context is given in Geiger et al. (2005).

Table 4 - Coefficients for the parametrization of the TOC reflectance factor uncertainty estimates.

	0.6 μm	0.8 μm	1.6 μm
c_1	0.001	0.005	0.000
c_2	0.07	0.02	0.04

For the inversion process it is taken into account all reflectance observations whose solar zenith angle and view zenith angle fall within an acceptable range limited by a maximum value of 85° . In order to further decrease the weight for reflectance measurements taken at extreme angles close to this limit, the zenith angles are scaled in the calculation of the relative air-mass in the following way:

$$\eta(\theta_{vj}, \theta_{sj}) = \frac{1}{2} \left(\frac{1}{\cos \theta_{vj}} + \frac{1}{\cos \theta_{sj}} \right) \text{ with } \tilde{\theta}_{vj} = \theta_{vj} \frac{90^\circ}{85^\circ} \text{ and } \tilde{\theta}_{sj} = \theta_{sj} \frac{90^\circ}{85^\circ}. \quad (32)$$

The rationale of this prescription is the potential systematic problems in the atmospheric correction for very large solar and view angles, for which the employed scheme was not specifically designed, as well as the divergence of the f_1 geometric kernel function (cf. Figure 3).

4.3.4 Illustration of the model inversion

In order to illustrate the functioning of the model inversion approach, Figure 4 depicts an example for the series of atmospherically corrected reflectance factor values obtained from the SEVIRI image slots acquired during one day as a function of the solar zenith angle. The bars attached to each data point (from the center to each end) correspond to the uncertainty estimates used in the weighting scheme. Data points flagged as of bad quality in the cloud mask are marked in gray color. Image slots for which the considered pixel was flagged as cloudy are marked with a rhombus symbol at the abscissa. In this example this occurs for a number of slots close to local solar noon at a zenith angle of roughly 26° . The solid lines in the graphs represent the result obtained by re-calculating the reflectance factor with Equation (24) from the retrieved best-fit model parameters in the same geometric configuration as the observations.

The interest of the model fit for albedo determination is to obtain an interpolation and extrapolation of the reflectance factor for geometric configurations that are not observed. For one of the spectral channels of the example case, Figure 4 depicts the modeled reflectance factor for different illumination directions. The graphs show that the angular dependence becomes increasingly important for large incidence angles.

Top and bottom panels of Figure 4 respectively show the principal and orthogonal planes which correspond to the vertical and horizontal sections of the polar graph shown on the right hand side of Figure 2. For the top panels negative values of the zenith angle θ_{out} correspond to the back scattering direction ($\varphi = 0^\circ$) and positive values to the forward scatter direction ($\varphi = 180^\circ$). The bottom panels, which are symmetric in θ_{out} , correspond to relative azimuth angles $\varphi = 90^\circ$ and $\varphi = 270^\circ$.

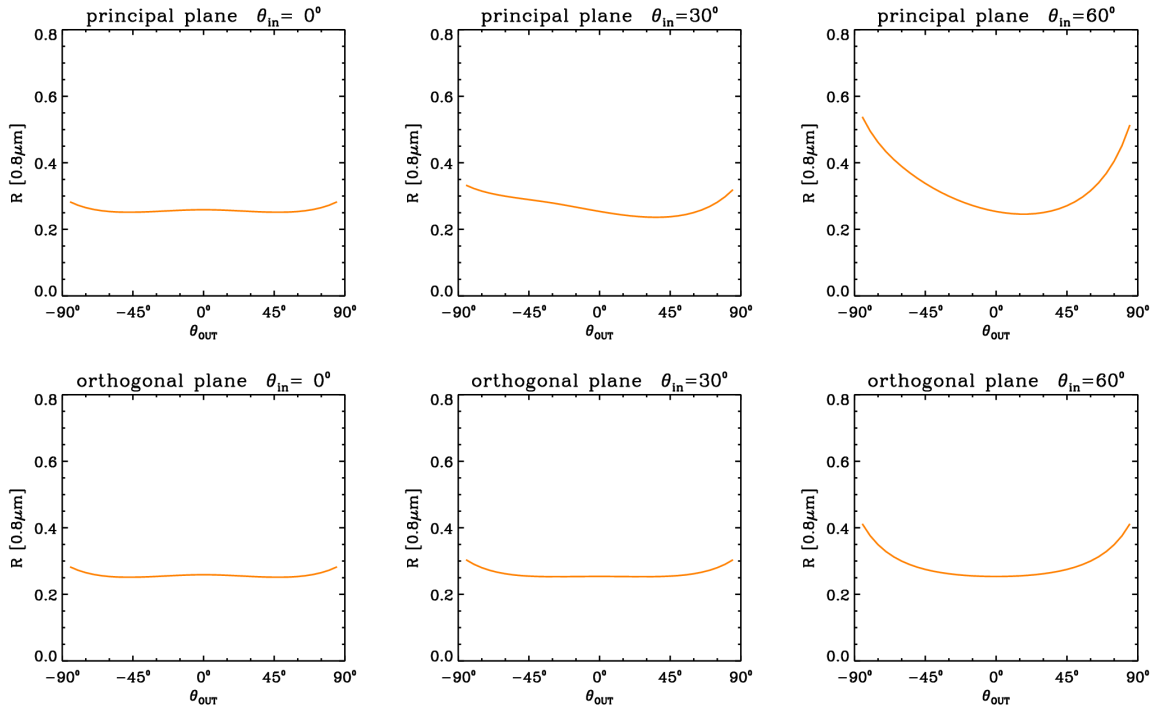


Figure 4: Dependence of 0.8 μm reflectance factor on the direction of the outgoing light ray for different incidence directions according to the model of uncertainty.

4.3.5 Temporal Composition

In order to reduce the sensitivity of the resulting daily estimates to reflectance outliers and extended periods of missing data because of persistent cloudiness, it is necessary to combine the information over a longer time period. A recursive scheme is applied for this purpose. At each execution of the algorithm the previous parameter estimate \mathbf{k}_{in} and the corresponding uncertainty measure \mathbf{k}_{in} is read from the relevant internal product files. Since these quantities now serve as input information, the index “in” is added to the symbols in order to distinguish them from the new estimates to be derived. The previous estimates are then used in the following way as a priori information for the linear model inversion specified in Equations (22) and (23):

$$\mathbf{k}_{\text{ap}} = \mathbf{k}_{\text{in}} \quad (33)$$

$$\mathbf{C}_{\text{ap}} = \mathbf{C}_{\text{k}}^{\text{in}} (1 + \Delta)^{(t_0 - t_{\text{in}}) / \Delta t} \quad (\text{with } \Delta t = 1 \text{ day}).$$

The multiplicative factor (larger than one) applied to the covariance matrix reduces the confidence in the a priori estimate as a function of the lapse of time $t_0 - t_{\text{in}}$ since the previous execution of the algorithm. The result of the inversion, constrained in this way with a priori information obtained from previous observations, is mathematically equivalent to performing the inversion directly with the complete set of observations by attributing less weight to those observations acquired before the day t_0 . A multiplicative factor in the weights translates into the inverse of the square root of this factor in the elements of the covariance matrix resulting from the model

inversion. The recursive multiplication process can therefore be identified with the presence of an effective temporal weight function [cf. Equation (27)] of the form

$$\begin{aligned}
 w_t(t) &= (1 + \Delta)^{-(t_0-t)/(2\Delta t)} \quad \text{for } t \leq t_0, \\
 w_t(t) &= 0 \quad \quad \quad \text{for } t > t_0,
 \end{aligned}
 \tag{34}$$

which is shown in Figure 5. The quantity Δ can be related to the characteristic temporal scale τ (full width at half mean) of this weight function. This parameter is chosen as 10 days in the present configuration of the algorithm running in the operational system for AVHRR. When proceeding like this, it gives to past products a weight of 50% after 10 days and only 10% after 20 days. This value represents a satisfactory compromise between temporal resolution and sensitivity to remaining small scale variations in the reflectance factor values which are due to uncorrected atmospheric effects.

If no new observations are available during the whole day due to persistent cloudiness, the estimate for the model parameters \mathbf{k} remains unchanged and only the multiplicative factor is applied for the covariance matrix as in Equation (34). The “age” of the last observation exploited in the recursive inversion scheme is an important piece of information for potential applications and is therefore also made available to the users. As for AVHRR, are considered composite periods of 20 days and synthetic periods of 10 days. The aging of the ETAL is taken as a the mean value of the dates of the clear scenes used to generate the ETAL product.

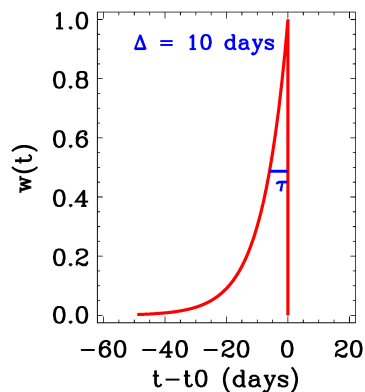


Figure 5: Effective temporal weight function in the recursive composition scheme. The characteristic time scale is $\tau = 10$ days for AVHRR.

In line with the real-time strategy of LSA SAF the implemented method makes it possible to deliver the best estimate of the state of the land surface at the time of product generation and distribution by giving the largest weight to the most recent observations. At the same time owing to the successive accumulation of information a complete spatial coverage is achieved without the need for static surface information databases. The implemented recursive composition scheme is similar to a Kalman filter without intrinsic time evolution of the model (cf. Samain, 2005).

4.3.6 Angular Integration

Inserting the reflectance model [Equation (12)] in the albedo definitions [Equations (5) and (6)] gives the expressions

$$a_{\beta}^{dh}(\theta_{in}) = k_{\beta} \mathbf{I}^{dh}(\theta_{in}) \quad \text{and} \quad a_{\beta}^{bh} = k_{\beta} \mathbf{I}^{bh}, \quad (35)$$

for the spectral albedo quantities, where

$$I_i^{dh}(\theta_{in}) = \frac{1}{\pi} \int_0^{2\pi} \int_0^{\pi/2} f_i(\theta_{out}, \theta_{in}, \varphi) \cos(\theta_{out}) \sin(\theta_{in}) d\theta_{out} d\varphi \quad (36)$$

$$\text{and} \quad I_i^{bh} = 2 \int_0^{\pi/2} I_i^{dh}(\theta_{in}) \cos(\theta_{in}) \sin(\theta_{in}) d\theta_{in},$$

are the respective angular integrals of the fixed kernel functions which can conveniently be precomputed and stored in look-up tables. Figure 6 shows the illumination angle dependence of the directional-hemispherical integrals of the three kernels according to the model introduced by Roujean et al. (1992), which is currently used in the operational system.

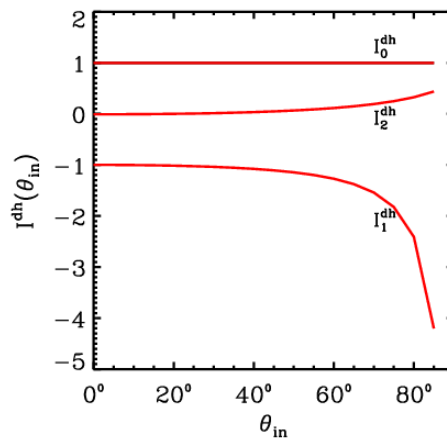


Figure 6: Illumination zenith angle dependence of the directional-hemispherical kernel integrals for the Roujean et al. (1992) model.

Thanks to the linear relationship [Equation (35)] between the BRDF model parameters and each of the spectral albedo quantities, standard uncertainty estimates for the latter can conveniently be derived from the respective uncertainty covariance matrix \mathbf{C}_k of the model parameters (cf. Lucht and Lewis, 2000) and the appropriate kernel integrals \mathbf{I} :

$$\sigma[a] = \sqrt{\mathbf{I}^T \mathbf{C}_k \mathbf{I}} \quad (37)$$

Figure 7 shows the dependence of the directional-hemispherical albedo on the illumination zenith angle according to the result of the model fit for the example case discussed in Section 4.3.4. In the graphs an increase of a^{dh} with rising θ_{in} can be noticed which is characteristic for most types of land surfaces.

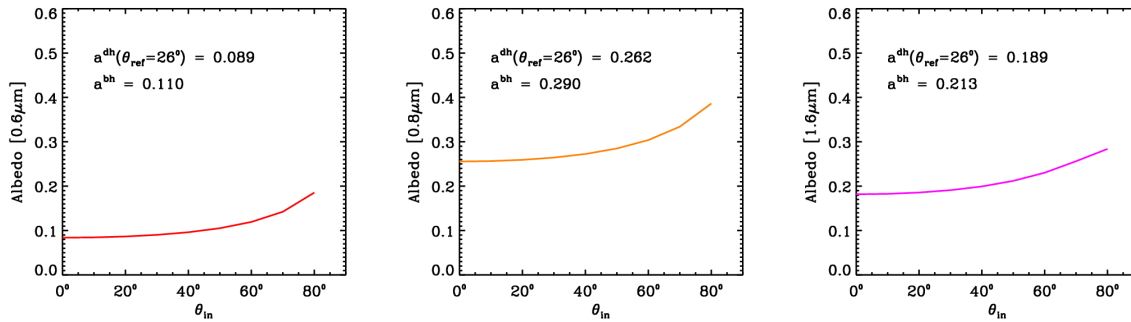


Figure 7: Dependence of the directional-hemispherical albedo on the illumination zenith angle. The value at the reference angle θ_{ref} and the bi-hemispherical estimate are indicated.

The LSA SAF albedo product files are the directional-hemispherical albedo $a^{dh}(\theta_{ref})$ for a specific reference angle θ_{ref} and the bi-hemispherical albedo a^{bh} . The solar position at local noon was chosen for the former product as the directional reference, which means that the zenith angle θ_{ref} is determined as a function of each pixel's geographic coordinates and the day of the year. For the time being the information on the complete functional dependence $a^{dh}(\theta_{in})$ is not available in the (external) product files. Appropriate empirical formulas (e.g., Dickinson 1983, Briegleb et al. 1986) may be applied for modeling the evolution of directional-hemispherical albedo $a^{dh}(\theta_s)$ according to the daily solar cycle. Finally, Equation (7) can be applied to calculate a weighted average of the directional and bi-hemispherical estimates as a function of the fraction of diffuse radiation to approximate a real sky situation.

As it can be seen from Figure 6, the directional-hemispherical integral $I_1^{dh}(\theta_{in})$ of the used kernel function f_1 tends to diverge as the illumination zenith angle approaches 90° . This may lead to a potential problem for the directional-hemispherical albedo when the illumination zenith angle is very large. However, the numerical values of the parameter k_1 are usually one order of magnitude smaller than k_2 , which mitigates the apparent dominance of the f_1 kernel in the angular dependence of the integrals $I_i^{dh}(\theta_{in})$. In the algorithm an upper limit of 85° is specified for the reference angle θ_{ref} in the calculation of the directional-hemispherical albedo variant. Also, under such conditions the fraction of diffuse radiation becomes dominant, and the directional-hemispherical albedo is then of little

relevance for practical purposes. Owing to the weighting with the cosine of the illumination angle in the bi-hemispherical integral of Equation (36), the divergence of $I_1^{dh}(\theta_{in})$ is no problematic for the bi-hemispherical albedo variant.

4.4 Narrow- to Broad-band Conversion

The kernel approach offers a description of the angular dependence of the reflectance factor. It is applied to each instrument channel separately and provides no information on the spectral behavior outside of the available narrow bands. Broad-band albedo is defined as the integral of spectral albedo over a certain wavelength interval weighted by the spectral irradiance [cf. Equations (10) and (11)]. Since the integral can be approximated as a weighted sum of the integrand at discrete values of the integration variable, broad-band albedo may be expressed as a linear combination of the spectral (or rather narrow-band) albedo values in the available instrument channels.

The algorithm the broad-band albedo estimates for a given target interval γ are derived from the spectral quantities by applying a linear transformation of the form

$$a_\gamma = c_{0\gamma} + \sum_{\beta} c_{\beta\gamma} a_\beta \quad (38)$$

with coefficients $c_{0\gamma}$ and $c_{\beta\gamma}$ as summarized in Table 5. Three different broad-band albedo intervals are considered: the total short-wave range from 0.3 μm to 4 μm , the visible wavelength range from 0.4 μm to 0.7 μm , as well as the near infrared range from 0.7 μm to 4 μm .

The narrow- to broad-band conversion coefficients were determined by *van Leeuwen and Roujean (2002)*. Those authors performed a linear regression analysis based on radiative transfer simulations. They generated an extensive data set of synthetic spectral canopy reflectances for different surface types by using the ASTER spectral library (Hook, 1998) and the SAIL radiative transfer model (*Verhoef, 1984*). After calculating the narrow-band albedo values in the AVHRR instrument's spectral bands and the broad-band albedo values in the ranges of interest, they then determined the corresponding linear transformation coefficients.

Table 5 - Narrow- to broad-band conversion coefficients for the AVHRR channels (*van Leeuwen and Roujean, 2002*).

γ	$c_{0\gamma}$	$c_{1\gamma}$ (0.6 μm)	$c_{2\gamma}$ (0.8 μm)	$c_{3\gamma}$ (1.6 μm)
[0.3 μm , 4 μm]	0.003880	0.5234	0.3102	0.1097
[0.4 μm , 0.7 μm]	0.008367	0.9642	0.0454	-0.1193
[0.7 μm , 4 μm]	-0.001224	0.0861	0.5738	0.3521

The spectral properties of snow are rather different from those of ordinary land surfaces and the narrow- to broad-band conversion cannot be well described with the same linear relation. For pixels flagged as snow-covered in the CMA cloud mask product we therefore use the different set of coefficients listed in Table 6, which were determined with a similar regression analysis as described above.

Table 6 - Narrow- to broad-band conversion coefficients for pixels flagged as snow-covered for AVHRR calculated with tools developed by *Samain (2005)*.

γ	$c_{0\gamma}$	$c_{1\gamma}$ (0.6 μm)	$c_{2\gamma}$ (0.8 μm)	$c_{3\gamma}$ (1.6 μm)
[0.3 μm , 4 μm]	0.0254	0.3807	0.3844	0.0251
[0.4 μm , 0.7 μm]	0.0068	0.9996	-0.0006	0.0000
[0.7 μm , 4 μm]	0.0222	0.0265	0.5808	0.3475

The weighting with the spectral irradiance in the definition of the broad-band albedo introduces a dependence on the atmospheric conditions since the spectral properties of the downward irradiance are different under direct and diffuse conditions. For the time being this difference is not taken into account in the generation of the input data sets for the regression analysis and the same narrow- to broad-band conversion relations are applied for the directional-hemispherical albedo $a^{dh}(\theta_{ref})$, irrespective of the reference illumination angle, and for the bi-hemispherical albedo variant.

Assuming that the errors of the spectral albedo estimates are uncorrelated, the uncertainty estimate for the broad-band albedo quantities is given by

$$\sigma[a_\gamma] = \sqrt{\sigma_{\text{Regression}}^2 + \sum_{\beta} (c_{\beta\gamma})^2 \sigma^2[a_\beta]} \quad (39)$$

where $\sigma_{\text{Regression}}^2 = 0.01$ denotes the estimated residual variance of the linear regression.

4.5 Signification of the Uncertainty Estimates

The (theoretical) uncertainty estimates for the respective albedo quantities represent the most general quality indicator operationally delivered by the algorithm. They are calculated for each pixel as a function of the respective observation conditions. The validity of these estimates is strictly speaking restricted to the framework of the applied BRDF model and their quantitative pertinence needs to be checked with appropriate validation studies.

Determining the best solution of the linear model inversion problem in a least square sense implicitly includes the assumption that the probability distributions of the errors of the TOC reflectance factor values are Gaussian and mutually uncorrelated, that is their uncertainty covariance matrix $\mathbf{C}_R = \text{diag}(\sigma^2[R_1], \dots, \sigma^2[R_n])$ is diagonal. In practice correlated errors may occur owing to instrument calibration uncertainties and systematic biases in the applied atmospheric correction scheme (or in the estimates of the concentration of atmospheric constituents used as input quantities for the correction). The uncertainty covariance matrix obtained for the model parameters therefore only quantifies the uncertainties due to the non-correlated (random) part of the input observation error structure.

When a large number of observations are available during clear periods the respective uncertainties for the model parameters become formally very small, which indicates that the model is then very well constrained. The albedo is calculated from the model parameters by linear expressions and the albedo uncertainty estimates are obtained by propagating those of the model parameters. Hence the albedo uncertainty estimates preserve the formal Gaussianity and they also reflect uncertainties due to the non-correlated part of the reflectance error structure while correlated (systematic) errors are not taken into account. The instrument calibration uncertainty may be taken into account a posteriori in a simplified way by “root-sum-squared-addition” to the delivered albedo uncertainty estimates.

With the implementation of the recursive temporal composition method, the uncertainty estimates also express the temporal aspect of the relevance of the observations. In periods without useful observations the uncertainty increases. This reflects the decreasing confidence in the parameter estimate due to “ageing” of the information on which the estimate is based.

Non-Gaussian outliers in the reflectance observations owing to undetected clouds cause another potential problem for the uncertainty treatment. Imperfections in the cloud screening method can lead to a significant contribution of outliers in the probability density distributions of the top-of-canopy reflectance errors. This can affect the quality of the inversion results as well as the validity of the uncertainty estimates. Nevertheless, the strategies employed for penalizing or eliminating potentially unreliable observations reduce the importance of this problem.

4.6 The CAMS climatology used for aerosols correction

The aerosol correction will make use of the data sets from CAMS (Copernicus Atmosphere Monitoring Service) in the future. The CAMS products are in particular validated against MODIS AERONET stations.

The CAMS data set are used first to generate a new climatology of aerosol properties using MACC-II reanalysis product for 0.125 degree resolution.

The aerosol optical depth (AOD) at five wavelengths namely, 469, 550, 670, 865 and 1240 nm are available for a 10 years period (2003 to 2012) on a monthly basis with 3 time step (6, 12, 18) per day. So for one month say January, the total record length is $(10 \times 31 \times 3)$ that is 930. The records may change based on the month of choice. The files are in netCDF format.

The longitude (lon) of the data set starts with 0 degrees and with a step of every 0.125 degrees ends at 359.875 degrees. The dimension of this data set is 2880 values. The latitude (lat) of the data set starts with -90 degrees and ends at 90 degrees with a step of 0.125 degrees. The dimension of this data set is 1441 values.

Hence, the AOD data set has a shape of 930 X 1441 X 2880 dimension (time X lat X lon). The grid projection is Plate Carrée. The Angstrom exponent (AE) is computed using AOD at all 5 wavelengths. AE is computed for each month and time step iterating over each pixel position.

A colour contour image of AOD for September 6h at wavelength 865 nm is shown (Figure 8.)

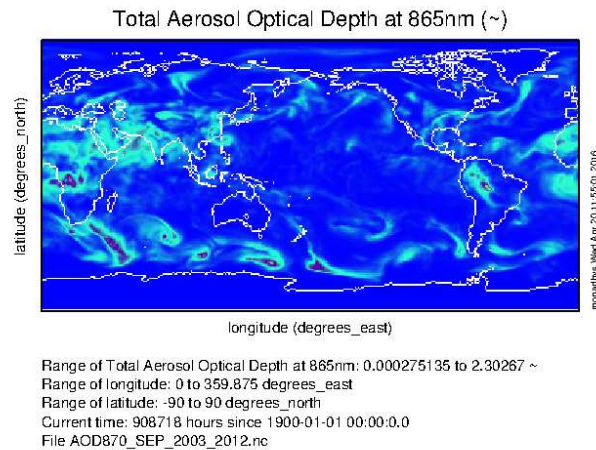


Figure 8: The colour contour image of CAMS climatology of AOD for September 6 h. The image is on a projected grid 0° West to 360° East and -90° South to 90° South.

4.7 Residual effect of cloud masking

In order to reduce the sensitivity to outliers due to undetected clouds, observations are eliminated from the analysis if the considered pixel is marked as cloudy in the CMA product in the slot acquired directly before or afterwards. In addition, observations for which the respective flag of the cloud mask product CMA indicates a bad quality are penalized in the weighting scheme by multiplying the reflectance uncertainty estimate by a factor 10. The same approach is adopted for the observations of pixels that might be contaminated by cloud shadows according to their location next to cloudy pixels and considering the solar azimuth direction. In this way the potentially affected observations are only significant in the inversion process if no “reliable” observations are available at all.

The contamination by sub-pixel cloud (low broken merely) is difficult to appraise because the effect at such resolution is similar to thin clouds (cirrus) or some aerosol (smoothing of the information). The cloud classification used does not mention the cloud type. Thus, the strategy here, which is similar to SEVIRI and AVHRR, considers a severe application of the CMA product in discarding neighbour pixels near cloudy pixels due to shadowing as aforementioned plus a systematic dilatation of cloud mask. As for MSG/SEVIRI, a pixel is discarded if it was acquired within 2 slots surrounding a scene for which the pixel was declared cloudy.

Up to version AL2 v5.0, the albedo algorithm considers all observations declared as cloud-free by the cloud mask software, to say the CMA product from NowCasting SAF. However, it was found that some cloud contaminated pixels still remain, which may have led to spurious variability on short time scales in the resulting albedo estimates. Therefore, a more ‘agressive’ technique to filter cloudy pixels has been implemented. It consists to discard a pixel plus two other pixels corresponding to slot

before and after, when the cloud mask of the NWC-SAF is judged dubious.

Moreover, clouds make shadows on cloud clear surfaces what causes no legitimate variations of albedo. A simple principle of decontamination is now used (see figure 9 below). The decontamination is function of azimuth position of the sun and eliminates just some pixels (not all), which are near a cloudy pixel.

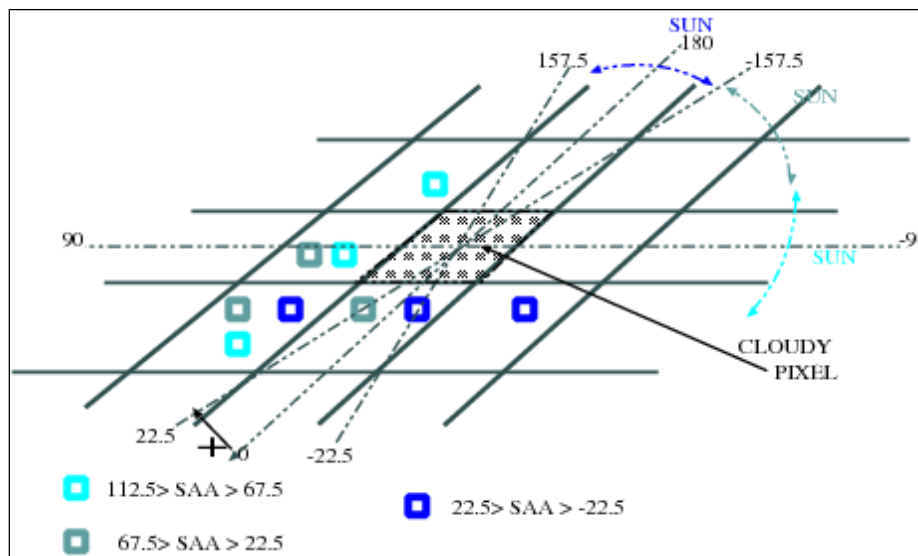


Figure 9: Sketch of the technique applied for the removal of cloud-contaminated pixels as a function of the solar geometry. Three examples are given here to discard nearest neighbour pixels (blue squares) relative to a cloudy pixel, according to the solar azimuthal position.

The following improvements have been implemented:

1. A bad quality flag in the cloud mask product (CMA product from NowCasting SAF) serves to discard pixels even marked as clear.
2. Further pixels are then eliminated due to cloud shadowing.
3. Further pixels are eliminated from observations directly acquired before or after a cloudy slot.

Worthy to mention that owing to the 15 minutes repeat cycle of MSG/SEVIRI a large number of slots are available. Thus, adopting a conservative approach for discarding some of them does not seriously compromise the information content available for generating the albedo product.

4.8 Synthesizing MDAL/MTAL and ETAL differences

The albedo products derived from SEVIRI and AVHRR are intended to be merged, particular MTAL and ETAL who are sharing the same temporal resolution. But MTAL product is expected to be more relevant than ETAL as it will include more updated information issued from MDAL. The differences and similarities are expressed here below through the prism of the various offered resolutions

4.8.1 Spectral resolution

The spectral response functions are very similar for VIS0.6 and VIS1.6 but shows differences for VIS08 for vegetation (Figure 10). In addition, VIS0.8 for AVHRR sees more atmospheric absorption compared to SEVIRI. Using an inter-satellite transfer function, *van Leeuwen and Roujean (2002)* have found that spectral albedos at VIS0.6 and VIS1.6 from SEVIRI and AVHRR could be compared with an accuracy of 0.002 and 0.004, respectively (standard error). This error is about 0.01 in albedo unit for VIS0.8. Note that narrow to broadband correction reduces this error staged as the relative weight given to the VIS0.8 channel.

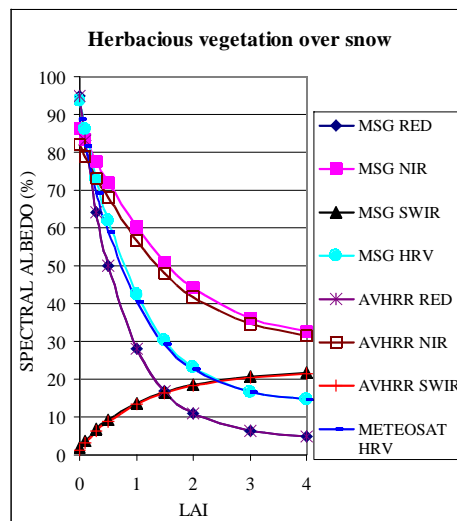


Figure 10: Comparison of the spectral albedo for SEVIRI and AVHRR from simulations using the SAIL code (*van Leeuwen and Roujean, 2002*).

4.8.2 Spatial resolution and projection

The dissemination of MDAL/MTAL considers the satellite projection and the nominal resolution. The pixel resolution is established as $3\text{km}/[\cos(\text{LAT}) \cdot \cos(\text{LON})]$. On the other hand, ETAL product is projected on a sinusoidal grid with a pixel size of 0.01° . Therefore, the inter-comparison of the albedo products from the two satellites is not straightforward and offered reprojection tools by the project should be used.

4.8.3 Directional resolution

GEO satellites like MSG/SEVIRI observe a given target under the same view zenith angle but at different time and thus under different sun zenith angles. This infers variations in the relative azimuth angles. At the opposite, a LEO satellite like Metop/AVHRR sees the same target under almost the same solar geometry within 10 days but with large variations of the view zenith angles and relative azimuth angles scanning both backward and forward close to the principle plane. As a result, different BRDF are obtained from GEO and LEO satellites and their complementarity is conspicuous. The Figure11 highlights this statement.

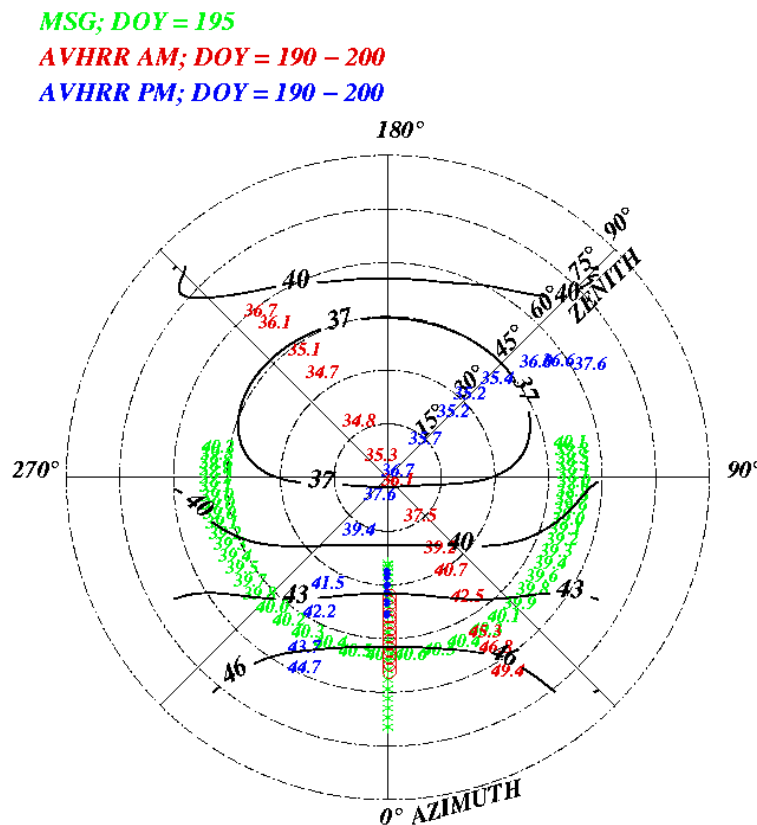


Figure 11: Directional sampling from GEO (MSG/SEVIRI) and LEO (Metop/AVHRR) satellites for the city of Toulouse (France) on July 14, 2010, with plus/less 5 days for LEO.

4.8.4 Temporal resolution

A different compositing technique is adopted between GEO and LEO satellites. Owing to potentially 96 observations over a single day, MSG/SEVIRI offers the possibility to estimate a daily surface albedo product, so-called MDAL. Besides,

MTAL is a 10-day product derived from a simple average of MDAL. The date associated to MDAL corresponds to the middle of the 10-day period.

As for Metop/AVHRR, the strategy to derive the 10-day surface albedo product ETAL is different than for MTAL. A compositing period of 30 days is considering within which the maximum of clear pixels is retained to proceed to model inversion. The date associated to ETAL also corresponds to the middle of the 10-day period.

Note that MDAL (LSA-101) is better appropriate to capture short timescale variations compared to MTAL (LSA-102) or ETAL (LSA-103).

5 Known issues and limitations

The factors limiting the quality of the ETAL product are of three categories.

1. *Residual of clouds and subpixels clouds* – This issue is however difficult to quantify at the level of the LSA SAF project in the lack of detailed nomenclature on cloud classification. Thus, the strategy of LSA SAF was to be rather severe in discarding the potential outliers pixels for two slots before and after a cloud contaminated pixel. Following the same idea, pixels surrounding a cloud contaminated pixel are discarded by adoption of the strategy of dilatation of the cloud mask.

2. *Aerosol correction* – The CAMS product will be definitively adopted. For time being, a climatology was built but using near real time (NRT) CAMS to perform an aerosol correction is in our scope. Though somewhat challenging for the time being, it will reinforced the consistency between the Copernicus products at the benefit of the users. Note that same source of NRT information, MACC, was used to build the climatology although it may relate to different versions.

The simulated CAMS product has improved owing to an assimilation of the MODIS deep blue product since September 2015. On going cross-comparison against AERONET anchor stations are achieved and reported in a Quarterly Report (QR). The last results appear in Figure 12, which is extracted from this report. Due to some persistent bias on NRT CAMS, CAMS climatology to be used for the present time with a possibility for switching to NRT CAMS in the near future in watching QR.

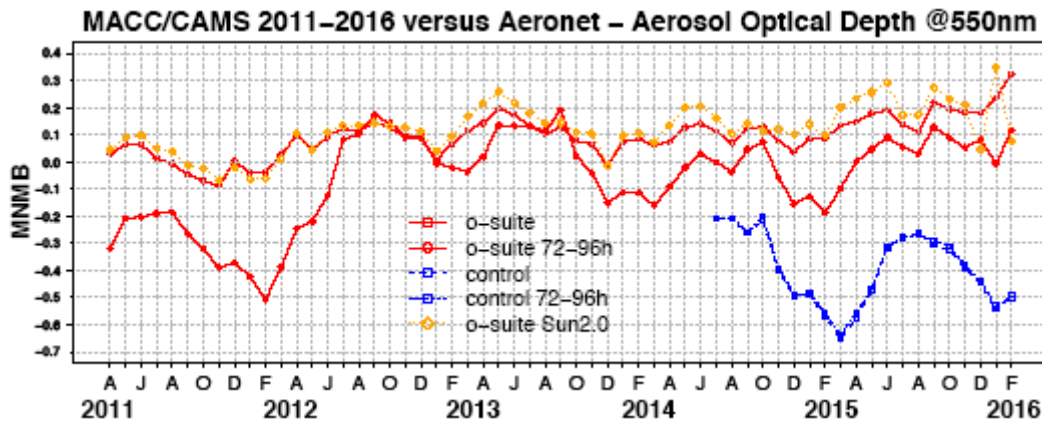
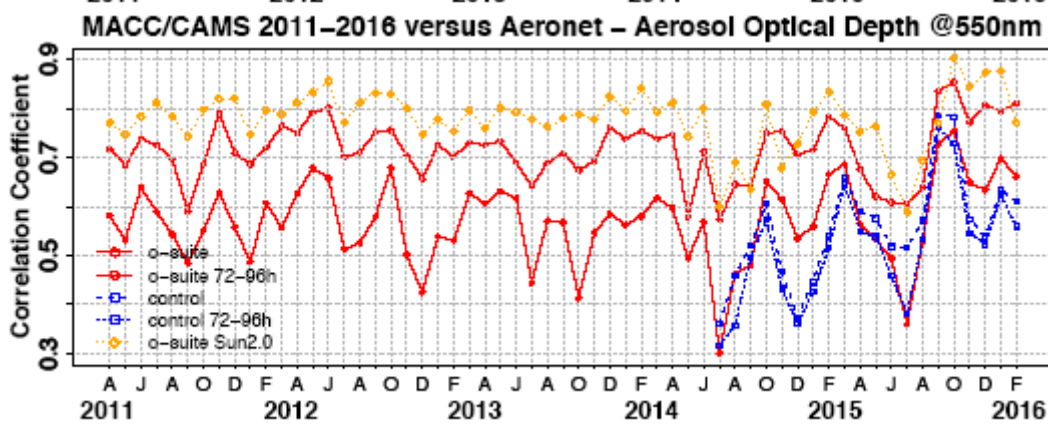


Fig
daily
(MN
dash
qual
coef
3. ;
proc
for i
is di
free



inst
bias
blue
inst
tion
[AL
uth
ors
ow-
to

better answer to users requirements and follows MODIS options.

For time being, the comparison of NIR ETAL product with MODIS in particular shows important discrepancies compared to the VIS ETAL product. Such deviations are still under investigation such like the NIR ETAL product would better satisfy to the users requirements in term of specifications.

6 References

- Barnsley M.J., Strahler A.H., Morris K.P., and J.P. Muller, 1994, *Sampling the surface bidirectional reflectance distribution function (BRDF): Evaluation of current and future satellite sensors*, *Remote Sensing Reviews*, 8, 271-311.
- Berthelot B., Dedieu G., Cabot F., and S. Adam, 1994, *Estimation of surface reflectances and vegetation index using NOAA/AVHRR: Methods and results at global scale*, *Communications for the 6th International Symposium on Physical Measurements and Signatures in Remote Sensing*, Val d'Isère, France, Jan. 17-21, 1994.
- Berthelot B., 2001, *Coefficients SMAC pour MSG*, Noveltis Internal Report NOV-3066-NT-834.
- Briegleb B.P., P. Minnis, V. Ramanathan, and E. Harrison, 1986, *Comparison of Regional Clear-Sky Albedos Inferred from Satellite Observations and Model Computations*, *Journal of Applied Meteorology*, 25, 2, 214-226.
- Carrer, D., S. Lafont, J.-L. Roujean, J.-C. Calvet, C. Meurey, P. Le Moigne, I. Trigo : Incoming solar and infrared radiation derived from METEOSAT : impact on the modelled land water and energy budget over France, *J. Hydrometeorol.*, 13(2), 504-520, doi:10.1175/jhm-d-11-059.1, 2012.
- Carrer, D., C. Meurey, X. Ceamanos, J.L. Roujean, J.C. Calvet, et S. Liu, Dynamic mapping of snow-free vegetation and bare soil albedos at global 1 km scale from 10-year analysis of MODIS satellite products, *Remote Sensing of Environment*, 140, 420-432, 2014.
- Cedilnik, J., J.F. Mahfouf, D. Carrer, et J.-L. Roujean, Impact assessment of daily satellite derived surface albedo in a limited area NWP model, *Journal of Applied Meteorology and Climatology*, vol. 51, no. 10, 1835-1854, 2012.
- Derrien M., 2002, *Specifications Calibration SEVIRI*, SPEC/MSG/001 v1.3, 2002, Météo-France/CMS.
- Dickinson R.E., 1983, *Land surface processes and climate – Surface albedos and energy balance*, *Advances in Geophysics*, 25, 305-353.
- Diner D.J. et al. (16 authors), 1998, *Multi-angle imaging spectro-radiometer (MISR) instrument description and experiment overview*, *IEEE Transactions on Geoscience and Remote Sensing*, 36, 1072-1087.
- Ferranti, L. e P. Viterbo, 2006: The European Summer of 2003: Sensitivity of Soil Water Initial Conditions. *J. Climate*, 19, 3659-3680.
- Geiger B., Hagolle O., and P. Bicheron, 2005, *CYCLOPES-Project: Directional Normalisation, Algorithm Theoretical Basis Document*, version 2.0.
- Hagolle O., Lobo A., Maisongrande P., Cabot F., Duchemin B., and de Pereyra A., 2004, *Quality assessment and improvement of temporally composited products of remotely sensed imagery by combination of VEGETATION 1 & 2 images*, *Remote Sensing of Environment*, 94, 172-186.

- Hook S. J., 1998, ASTER Spectral Library. <http://speclib.jpl.nasa.gov>
- Hu B., Lucht W., Li X., and A.H. Strahler, 1997, *Validation of kernel-driven models for global modeling of bidirectional reflectance*, Remote Sensing of Environment, 62, 201-214.
- Justice C.O. et al. (23 authors), 1998, *The Moderate Resolution Imaging Spectroradiometer (MODIS): Land remote sensing for global change research*, IEEE Transactions on Geoscience and Remote Sensing, 36, 1228-1249.
- van Leeuwen W. and J.-L. Roujean, 2002, *Land surface albedo from the synergistic use of polar (EPS) and geo-stationary (MSG) observing systems. An assessment of physical uncertainties*, Remote Sensing of Environment, 81, 273-289.
- Leroy M., Deuzé J.L., Bréon F.M., Hautecoeur O., Herman M., Buriez J.C., Tanré D., Bouffières S., Chazette P., and J.L. Roujean, 1997, *Retrieval of atmospheric properties and surface bidirectional reflectances over the land from POLDER/ADEOS*, Journal of Geophysical Research, 102(D14), 17023-17037.
- Li X., Gao F., Wang J., and A. Strahler, 2001, *A priori knowledge accumulation and its application to linear BRDF model inversion*, Journal of Geophysical Research, 106(D11), 11925-11935.
- Liu, S., J.L. Roujean, A. Kaptué Tchuenté, J.C. Calvet et X. Ceamanos, A parameterization of SEVIRI and MODIS daily surface albedo with soil moisture: calibration and validation over southwestern France, *Remote Sensing of Environment*, 144, 137-151, 2014.
- Lucht W. and P. Lewis, 2000, *Theoretical noise sensitivity of BRDF and albedo retrieval from the EOS-MODIS and MISR sensors with respect to angular sampling*, International Journal of Remote Sensing, 21, 1, 81-98.
- Lucht W. and J.L. Roujean, 2000, *Considerations in the parametric modeling of BRDF and albedo from multiangular satellite sensor observations*, Remote Sensing Reviews, 18, 343-379.
- Mitchell, K., et al., 2004: The multi-institution North American Land Data Assimilation System NLDAS: Utilizing multiple GCIP products and partners in a continental distributed hydrological modeling system, *J. Geophys. Res.*, 109, doi:10.1029/2003JD003823.
- Pinty B., Roveda F., Verstraete M.M., Gobron N., Govaerts Y., Martonchik J.V., Diner D.J., and R. A. Kahn, 2000a, *Surface albedo retrieval from Meteosat. 1. Theory*, Journal of Geophysical Research, 105(D14), 18099-18112
- Pinty B., Roveda F., Verstraete M.M., Gobron N., Govaerts Y., Martonchik J.V., Diner D.J., and R. A. Kahn, 2000b, *Surface albedo retrieval from Meteosat. 2. Applications*, Journal of Geophysical Research, 105(D14), 18113-18134
- Pokrovsky I.O., Pokrovsky O.M., and J.-L. Roujean, 2003, *Development of an operational procedure to estimate surface albedo from the SEVIRI/MSG observing system in using POLDER BRDF measurements*, Remote Sensing of Environment, 87, 198-242.

- Press W. H., Teukolsky S. A., Vetterling W. T., and B. P. Flannery, 1992, *Numerical Recipes in Fortran*, Cambridge University Press.
- Rahman H. and G. Dedieu, 1994, *SMAC: A simplified method for the atmospheric correction of satellite measurements in the solar spectrum*, International Journal of Remote Sensing, 15, 1, 123-143.
- Roujean J.-L., M. Leroy, and P.-Y. Deschamps, 1992, *A bidirectional reflectance model of the Earth's surface for the correction of remote sensing data*, Journal of Geophysical Research, 97(D18), 20455-20468.
- Samain O., 2005, *Fusion multi-capteurs de données satellitaires optiques pour la détermination de variables biophysiques de surface*, Ph.D.-Thesis, Université Paul Sabatier, Toulouse.
- Schmetz, J., P. Pili, S. Tjemkes, D. Just, J. Kerkman, S. Rota, and A. Ratier (2002), An introduction to Meteosat Second Generation (MSG), *Bull. Amer. Meteor. Soc.*, 83, 977-992.
- Sellers P.J., Mintz Y., Sud Y.C. and A. Duldres, 1986, *Simple Biosphere (SiB) Model for Use Within General Circulation Models*, J. Atm. Sci., 43, 505-531.
- Strahler A.H., 1994, *Vegetation canopy reflectance modeling - Recent developments and remote sensing perspectives*, Proceedings of the 6th International Symposium on Physical Measurements and Signatures in Remote Sensing, 593-600.
- Strahler A.H., Muller J.P. et al. (21 authors), 1999, *MODIS BRDF/Albedo Product: Algorithm Theoretical Basis Document*, version 5.0.
- Trigo, I. F., C. C. DaCamara, P. Viterbo, J.-L. Roujean, F. Olesen, C. Barroso, F. Camacho-de-Coca, D. Carrer, S. C. Freitas, J. García-Haro, B. Geiger, F. Gellens-Meulenberghs, N. Ghilain, J. Meliá, L. Pessanha, N. Siljamo, A Arboleda (2010), The Satellite Application Facility on Land Surface Analysis, *Int. J. Remote Sens.*, in press.
- Verhoef W., 1984, *Light scattering by leaf layers with application to canopy reflectance modeling, the SAIL model*, Remote Sensing of Environment, 16, 125-141.
- Wanner W., Li X., and A.H. Strahler, 1995, *On the derivation of kernels for kernel-driven models of bidirectional reflectance*, Journal of Geophysical Research, 100(D10), 21077-21090.
- Wanner W., Strahler A., Hu B., Lewis P., Muller J.-P., Li X., Barker-Schaaf C., and M. Barnsley, 1997, *Global retrieval of BRDF and albedo over land from EOS MODIS and MISR data: Theory and algorithm*, Journal of Geophysical Research, 102(D14), 17143-17161.

Appendix A. Developers

The development and implementation of the albedo algorithm have been carried out under the responsibility of the Centre National de Recherches Météorologiques (CNRM) de Météo-France (MF).

Authors: Bernhard Geiger, Dominique Carrer, Olivier Hautecoeur, Laurent Franchistéguy, Jean-Louis Roujean, Catherine Meurey, Xavier Ceamanos, and Gregoire Jacob

Appendix B. Glossary

AL:	Land Surface <u>A</u> lbedo <u>P</u> roduct
AVHRR:	<u>A</u> dvanced <u>V</u> ery <u>H</u> igh <u>R</u> esolution <u>R</u> adiometer
BRDF:	<u>B</u> i-directional <u>R</u> eflectance <u>D</u> istribution <u>F</u> unction
CNRM:	<u>C</u> entre <u>N</u> ational de <u>R</u> echerches <u>M</u> étéorologiques
CMA:	<u>C</u> loud <u>M</u> ask product developed by the NWC-SAF
cwv:	<u>c</u> olumn <u>w</u> ater <u>v</u> apour
CYCLOPES:	<u>C</u> arbon <u>C</u> ycle and <u>C</u> hange in <u>L</u> and <u>O</u> bservational <u>P</u> roducts from an <u>E</u> nsemble of <u>S</u> atellites
ECMWF:	<u>E</u> uropean <u>C</u> entre for <u>M</u> edium- <u>R</u> ange <u>W</u> eather <u>F</u> orecast
EPS:	<u>E</u> UMETSAT <u>P</u> olar <u>S</u> ystem
EUMETSAT:	<u>E</u> uropean <u>M</u> eteorological <u>S</u> atellite Organisation
GEO	<u>G</u> EOstationary
HDF:	<u>H</u> ierarchical <u>D</u> ata <u>F</u> ormat
IM:	<u>I</u> nstituto de <u>M</u> eteorologia (Portugal)
NIR:	<u>N</u> ear <u>I</u> nfrared Radiation
LEO	<u>L</u> ow <u>E</u> levation Orbit
LSA:	<u>L</u> and <u>S</u> urface <u>A</u> nalysis
METEOSAT:	<u>G</u> eostationary <u>M</u> eteorological <u>S</u> atellite
METOP:	<u>M</u> eteorological <u>O</u> perational polar satellites of EUMETSAT
MISR:	<u>M</u> ulti- <u>A</u> ngle <u>I</u> maging <u>S</u> pectra- <u>R</u> adiometer
MF:	<u>M</u> étéo- <u>F</u> rance
MODIS:	<u>M</u> oderate- <u>R</u> esolution <u>I</u> maging <u>S</u> pectro- <u>R</u> adiometer
MSG:	<u>M</u> eteosat <u>S</u> econd <u>G</u> eneration
NOAA:	<u>N</u> ational <u>O</u> ceanic and <u>A</u> tmospheric <u>A</u> dmistration (USA)
NWC:	<u>N</u> ow <u>C</u> asting
NWP:	<u>N</u> umerical <u>W</u> eather <u>P</u> rediction
PAR:	<u>P</u> hotosynthetically <u>A</u> ctive Radiation
POLDER:	<u>P</u> OLarization and <u>D</u> irectionality of <u>E</u> arth <u>R</u> eflectance
SAF:	<u>S</u> atellite <u>A</u> pplication <u>F</u> acility
SeaWifs:	<u>S</u> ea- <u>V</u> iewing <u>W</u> ide- <u>F</u> ield <u>S</u> ensor
SEVIRI:	<u>S</u> pinning <u>E</u> nhanced <u>V</u> isible and <u>I</u> nfrared <u>I</u> mager
SMAC:	<u>S</u> implified <u>M</u> ethod for the <u>A</u> tmospheric <u>C</u> orrection
TOC:	<u>T</u> op of <u>C</u> anopy
TOA:	<u>T</u> op of <u>A</u> tmosphere
PRD:	<u>P</u> roduct <u>R</u> equirements <u>D</u> ocument